Scientific report

on the project implementation in the period January 2012 – December 2015

1. „***Characterization of spin-coated TiO_2 buffer layers for dye-sensitized solar cells***”, J. Lungu, N. Ştefan, G. Prodan, A. Georgescu, A. Mandeş, V. Ciupină, I. N. Mihăilescu, M. A. Gîrţu, Digest Journal of Nanomaterials and Biostructures 10 (3) (2015) 967– 976

We report results on the fabrication and testing of dye-sensitized solar cells (DSSC) with spin coated TiO_2 thin films used as intermediate buffer layer between the conductive glass substrate and the nanocrystalline TiO_2 mesoporous layer. Our goal is to improve the DSSC characteristic parameters, such as the short circuit current density and the overall photovoltaic conversion efficiency.

The spin-coating technique is one of the most popular methods for applying thin uniform films onto flat surfaces. It is used frequently in photovoltaic research, due to its ease of use and relatively low cost, although it is not suitable for large-scale film processing. The spin-coating of the TiO2 sol–gel ethanolic solution was carried out in air with a spinning speed of 7000 rpm for 3 s. The precursor film formed following the deposition process was dried at 240ºC for 1 min on a hot plate. The spinning – drying cycle was repeated two, four, six, eight and ten times in order to get films of different thickness. The films with 2, 4, 6, 8, and 10 spin-coated layers were denoted T2X, T4X, T6X, T8X and T10X, respectively. After the deposition of last coating layer, the resulting film was annealed in air at 450ºC for 1 h and the thin TiO_2 surface was transparent and had a light-blue color.

The thicknesses of the spin-coated TiO2 films are reported as a function of the number of layers (see Fig. 1).

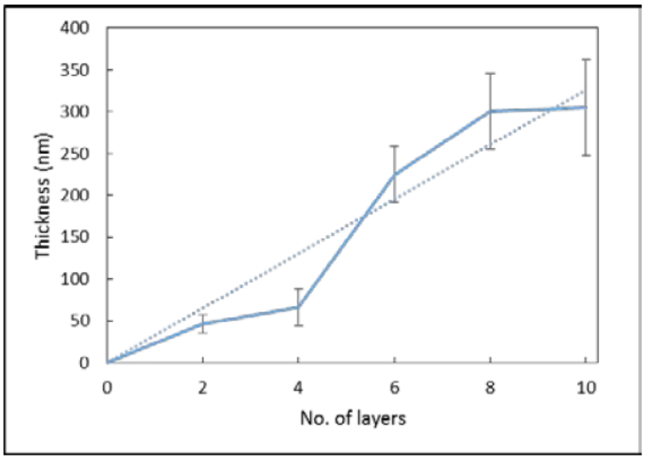

Fig. 1. The thickness of the TiO_2 buffer films as a function of the number of spin-coated layers. The dotted line is a linear fit

As expected, the film thickness after thermal treatment increases with the number of spin-coated layers, from about 47 nm for T2X to around 305 nm for T10X. Although the error of the thickness measurement is less than 2%, the large error bars displayed in Fig. 1 are due to the non-uniformity of the films, possible adherence problems, uneven solvent evaporation during the heating cycle (observed for such ZnO layers), etc. In any case, a correlation between the number of layers and the film thickness is obvious, the fit to a straight line leading to a slope of about 33 nm per layer.

Next, we studied the optical transmittance (Fig. 2) and absorbance spectra (Fig. 3) for the TiO_2 buffer layers. The lowest absorption throughout the visible range is recorded for T2X, whereas all other plates absorb starting from 350 nm (but T2X from Fig. 3 also seems to absorb starting at 350 nm). T10X plate spectrum shape is very similar to that for FTO, the difference in intensity between the two remaining almost constant for all wavelengths. At the UV-Vis limit, the other plates (T4X, T6X and T8X) absorb radiation in about equal measures. T8X plate has the best absorption in the ranges 450-520 nm, 610-690 nm and NIR (850-1200 nm), while for T6X the reverse situation is registered, as it absorbs only slightly better in the range 510-600 nm.

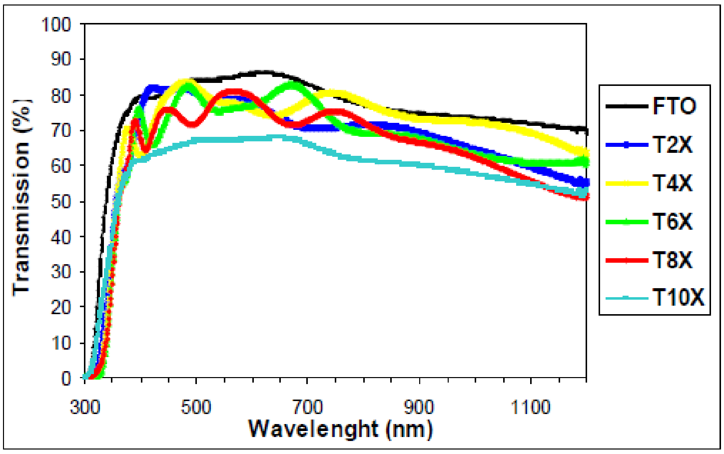

Fig. 2. The transmission spectra of the spin-coated TiO_2 buffer layers of various thicknesses, compared to the bare FTO glass

The steep decrease of the transparency in the near-UV region is caused by the strong light absorption in TiO_2, which is a wide bandgap semiconductor with the gap opening in the near UV, of about 3.2 eV. The wavelengths where the decrease in transmittance occurs are about 380 nm for all "TX" labeled plates, whereas for the FTO glass the wavelength is ~370 nm. The bandgap energy E_g of about 3.35 eV of the films was obtained by fitting the spectra to the equation of the absorption coefficient α, which is valid in the absence of the scattering effects and for allowed indirect optical transitions

$$\alpha \sim (E - E_g)^2,$$

where E is the photon energy. The slight increase in E_g may be correlated with finite size effects in the nanostructured photoelectrodes.

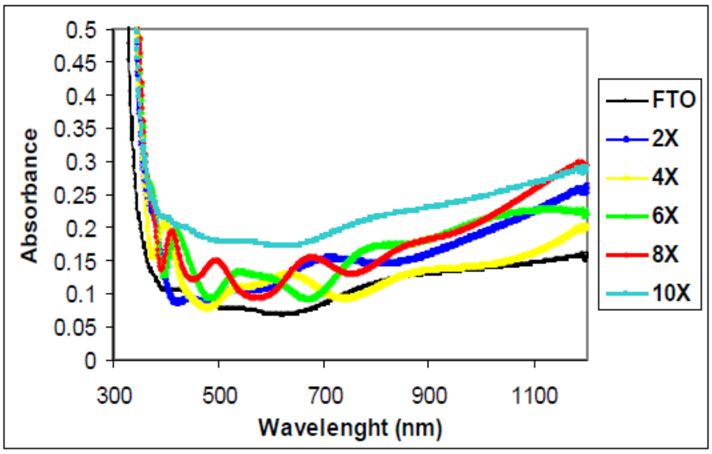

Fig. 3. The absorption spectra of the spin-coated TiO2 buffer layers of various thicknesses, compared to the bare FTO glass

Figs. 4-9 show transmission electron microscopy (TEM) images, grain size histograms (lognormal fitted), selected area electron diffraction (SAED) patterns and high transmission electron microscopy (HRTEM) images for the various spin-coated TiO_2 buffer layers. The grain sizes determined from TEM investigations are in the range of 6-30 nm for T6X TiO_2, with an average size of 13 nm (Fig. 4 inset), for T8X TiO_2 is in the range of 10-30 nm, with an average size of 15 nm (Fig. 6 inset) and of 18-75 nm for T10X TiO_2, with an average size of 27 nm (Fig. 8 inset). The associated SAED patterns and HRTEM images show the anatase structure of titania nanoparticles.

The SAED patterns for T6X, T8X and T10X films, presented in the insets of Figs. 5 7 and 9, show a very intense ring corresponding to reflection from (101) planes which indicates the anatase phase of nanocrystallites, but also some low intensity rings corresponding to reflections from other planes. Those images reveal also the values of interplanar distance of 0.355 nm for T6X, 0.351 nm for T8X and 0.348 nm for T10X, which are rather close to the standard anatase (101) plane (0.351690 nm). At a higher magnification, the TEM images of T6X, T8X and T10X samples exhibit both round shaped and elongated or facetted particles, by different sizes (Fig. 5, 7 and 9 respectively). Anatase phase nanocrystallites can be identified also from the 0.35 nm lattice fringes appearing in the same HRTEM images, which is in perfect agreement with SAED results.

Table 1 presents the comparative experimental values obtained for the distances between lattice planes in SAED analyzes, and the reference values for anatase TiO_2.

Table 1. Mean crystallite size, in nm, based on TEM investigations for the spin-coated layers

T6X	13.23 (±0.48)
T8X	14.68 (±0.61)
T10X	27.47 (±0.52)
mesoporos TiO_2	16.36 (±0.26)

The typical solar cell parameters resulting from the electro-optical measurements performed on DSSC fabricated on FTO as well as with various numbers of spin-coated buffer layers on FTO, are displayed in Table 2 whereas the I-V curves are illustrated in Fig. 10.

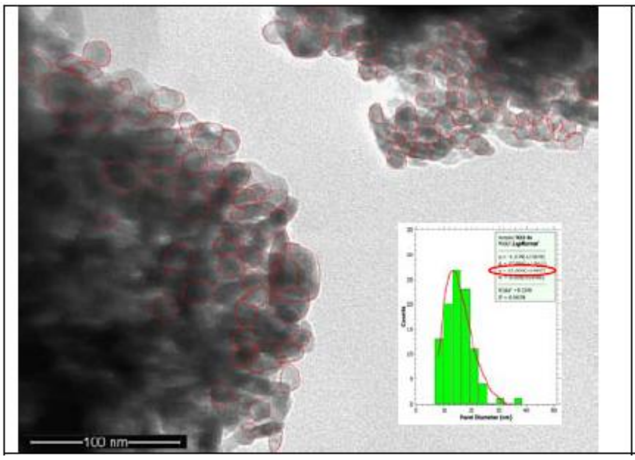

Fig. 4. TEM image with the distribution of grain size corresponding to six layers of TiO2 (T6X).

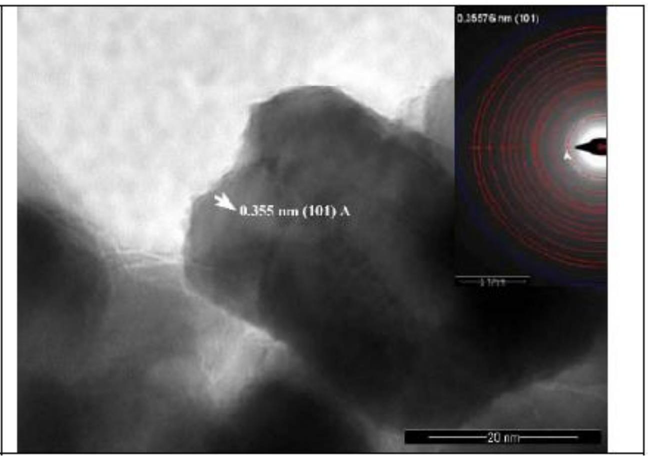

Fig. 5. HRTEM image and ELD patterns for (T6X)

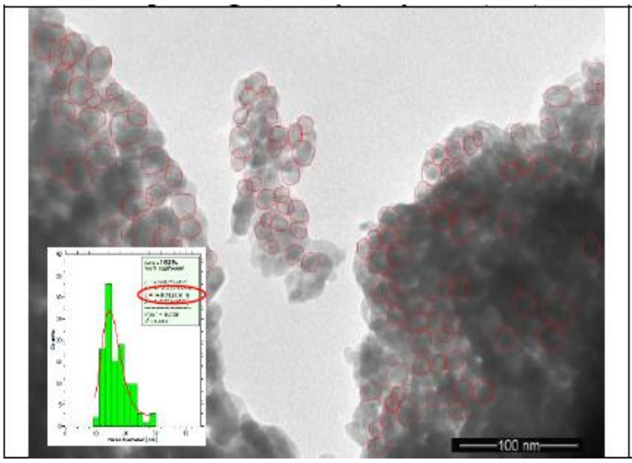

Fig. 6. TEM image with the distribution of grain size corresponding to eight layers of TiO_2 (T8X)

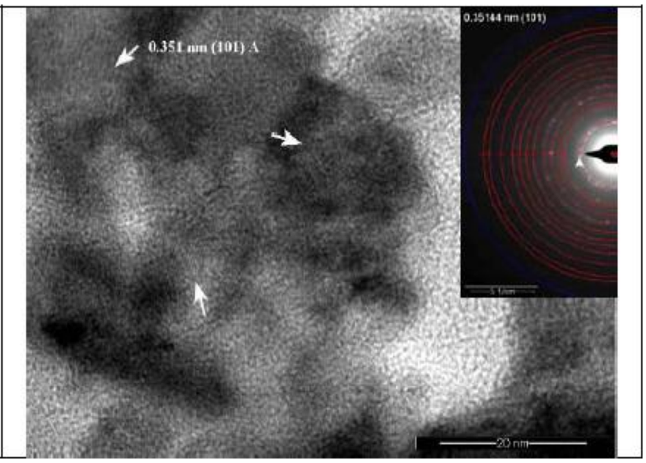

Fig. 7. HRTEM image and ELD patterns for (T8X)

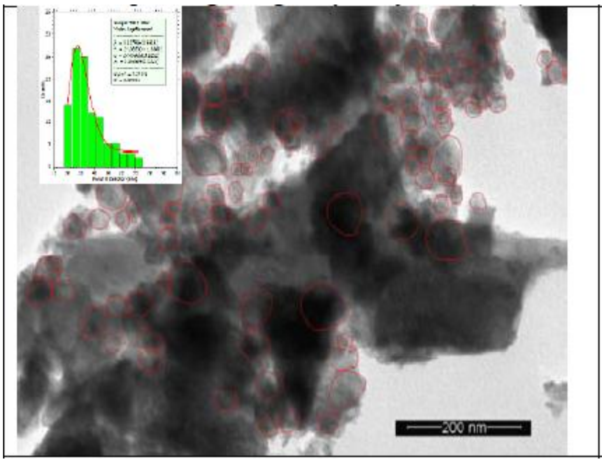

Fig. 8. TEM image with the distribution of grain size corresponding to eight layers of TiO_2 (T10X)

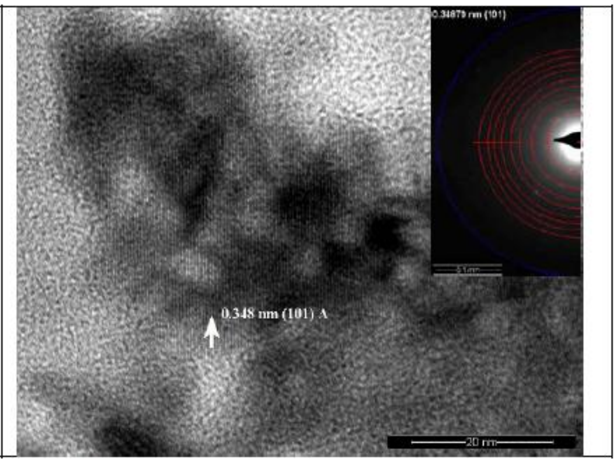

Fig. 9. HRTEM image and ELD patterns for T10X

Table 2. Electric parameters (open circuit voltage, Voc, short circuit current density, J_{sc}, maximum power, P_{max}, fill factor, FF, photovoltaic conversion efficiency, η) of typical DSSC measured under standard illumination conditions (see also Fig. 10)

Proba	V_{oc} (mV)	J (mA/cm^2)	P_{max} (μW)	FF	η (%)
without buffer layer	590	3.17	968.4	0.660	1.23
T2X	605	8.11	1850.4	0.480	2.36
T4X	602	8.08	1966.3	0.514	2.50
T6X	597	7.81	1836.5	0.502	2.34
T8X	611	8.28	2095.0	0.528	2.67
T10X	607	7.84	1962.6	0.525	2.50

The first observation is that the photovoltaic conversion efficiencies, *η*, obtained for DSSCs made with spin coated photo electrodes are between 2.38 % (for cells with 6 layers) and 2.67 % (for cells with 8 layers), which is almost twice the efficiency obtained for a cell without an intermediate layer. We note that the open-circuit voltage does not vary significantly. Therefore, crucial in determining the higher efficiency is the much larger short-circuit current density. The introduction of the buffer layer leads to an increasing of JSC, from 3.17 mA/cm^2 for cells without buffer layer, to 8.28 mA/cm^2 for T8X.

A second observation is that the filling factor is the highest for the device without a buffer layer. The I-V curves reveal a relatively high equivalent series resistance given by the slope of the curve when the current density approaches zero. The shunt resistance given by the slope close to the short-circuit current, which is almost horizontal, is high, as desired.

Finally, even though the differences between the various layer thicknesses are small, the better characteristics obtained for the T8X sample, with an efficiency of 2.67% suggest that there is an optimum buffer layer thickness.

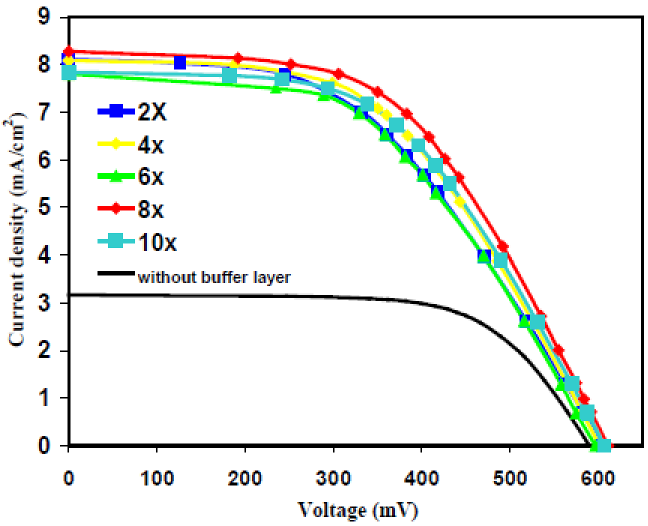

Fig. 10. Current-voltage curves for typical dye-sensitized solar cells fabricated with T2X (square), T4X (diamond), T6X (triangle), T8X (gray circle), T10X (empty circle) and without buffer layer (line) photoelectrodes

Electro-optical measurements carried out under standard AM 1.5G conditions showed that the introduction of a buffer layer at the interface increases significantly the short circuit current density and doubles the efficiency of the photovoltaic conversion with respect to the cells without the buffer layer. We proposed as an explanation of the better performance that the buffer layer improves the charge transfer and lowers the contact resistance at the FTO/TiO2 interface possibly by preventing the direct contact between the electrolyte and the FTO.

Encouraged by the present study we plan to expand our exploration of the role of the buffer layer on DSSC performance by using pulsed laser deposition instead of spin coating. If a simple method such as spin-coating can improve significantly the operation of the solar cell, the more uniform films obtained by means of laser deposition should lead to further improvements.

2. „***Surface-enhanced Raman scattering activity of niobium surface after irradiation with femtosecond laser pulses***”, Victor G. Ivanov, Emil S. Vlakhov, George E. Stan, Marian Zamfirescu, Catalina Albu, Natalia Mihailescu, Irina Negut, Catalin Luculescu, Marcela Socol, Carmen Ristoscu and Ion N. Mihailescu, Journal of Applied Physics 118 (2015) 203104

Niobium (Nb) is a technologically important metal with numerous industrial applications in metallurgy, electronics, medicine, superconducting magnets and radiofrequency cavities.

Niobium rods and plates were used for preparing discs of different thickness (up to 3 mm) and diameter (up to 8–10 mm). The Nb surface was irradiated by a linearly polarized fs laser beam with nearly Gaussian spatial profile. The ultra-short laser pulses were emitted by a Ti:Sapphire regenerative amplifier laser system (Clark-MRX, model CPA-2010) operated at a repetition rate of 2 kHz, with central wavelength at 775 nm and pulse duration of 200 fs. The sample surface was irradiated in ambient air at normal incidence using galvano-scanners (SCANLAB) and an f-Theta lens with 100 mm focal length as focusing optics. The waist of the focused beam was 37 μm, and the scanning direction was parallel to the laser polarization direction. The laser fluence was varied from 0.44 to 1.75 J/cm^2 and the scanning speeds were 0.5 mm/s and 4 mm/s. The size of the scanned areas was approximately (0.5 × 0.5) mm^2.

SEM comparative images of non-irradiated and irradiated areas of Nb samples are given in Fig. 11(a)–(h). Morphologically, the laser treatment performed at the lower scanning velocity and higher laser fluence resulted in evident surface roughening and the formation of well-separated slightly oblong islands of molten material with a size ranging between of ~2 – 10 μm, enclosed in a matrix with fine rippled structure having a lamellar (fringe-like) appearance (Fig. 11(a,e) characteristic to fs multipulse laser irradiation of almost any kind of materials, on surface or inside transparent bulk. The prominence of molten islands and consequently the ratio of the molten islands/rippled matrix areas, were generally increased when using the higher irradiation power (Fig. 11(*a*,*b*,*e*,*f*) vs. (*c*,*d*,*g*,*h*)).

EDS analyses indicated that besides the prevalent presence of Nb, cations of Al, Si, and Fe occur as impurities, with a concentration significantly decreasing after laser irradiation (Fig. 12). These contaminants can be due to the mechanical polishing of the Nb samples with SiC and Al_2O_3. The statistics of elemental composition within irradiated versus non-irradiated zones are given in Table 3. The significant increase of Nb concentration is confirmed along with the decrease of impurities after irradiation.

Table 3: Statistical elemental composition within laser irradiated and non-irradiated areas

Area	Composition (wt%)					
	Nb	O	C	Al	Fe	Si
Non-irradiated	56.72±0.78	19.45±0.22	11.06±1.25	8.18±0.08	4.19±0.26	0.4±0.05
Irradiated	66.25±0.27	19.3±0.16	8.76±0.4	4.58±0.3	0.92±0.08	0.19±0.07

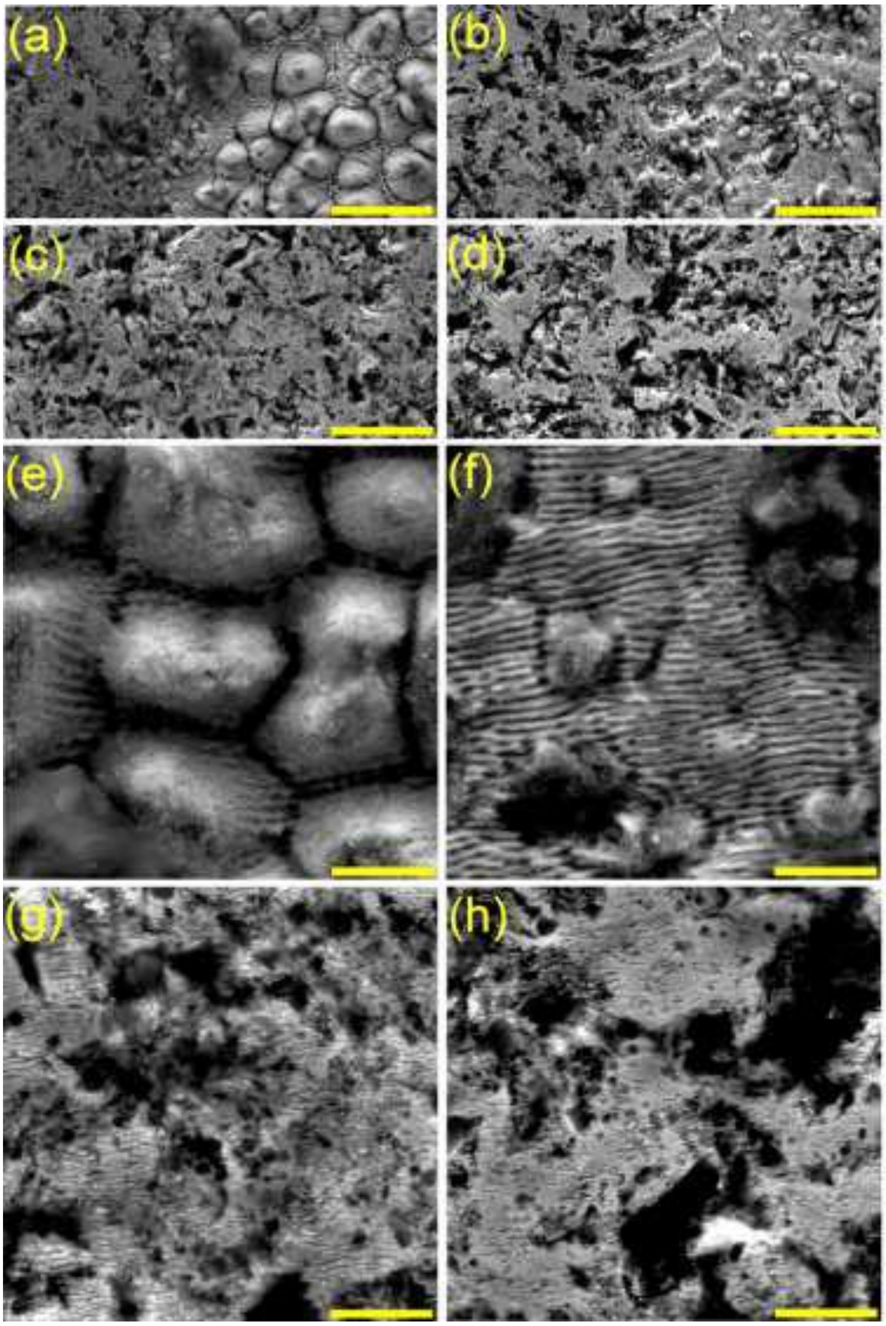

Fig. 11. SEM micrographs collected at two different magnifications: (a – d) bar=15 µm – surface morphological comparison at the separation limit between irradiated and non-irradiated surface; (e – h) bar=5 µm – detailed images of the irradiated areas, in the case of Nb disks treated at irradiation powers of 1.75 J/cm^2 (a,b,e,f) and 0.44 J/cm^2 (c,d,g,h), with a scanning velocities of 0.5 mm/s (a,c,e,g) or 4 mm/s (b,d,f,h).

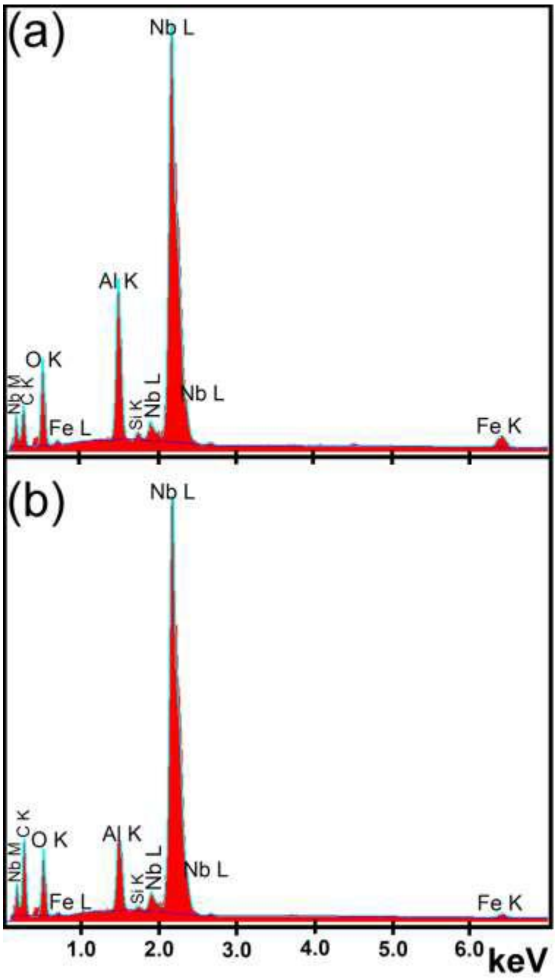

Fig. 12. Comparative EDS spectra of non-irradiated (a) and irradiated (1.75 J/cm^2 irradiation fluence, 0.5 mm/s scanning velocity) (b) Nb sample

We also performed mapping analysis (Fig. 13) of the entire sample surface - *i.e.* irradiated and non-irradiated areas which confirmed that irradiated spots contain mostly Nb and Al or Fe.

The AFM analyses (Fig. 14) pointed to an augmentation of the surface roughness when increasing the laser fluence. At a constant scan speed of 0.5 mm/s, R_{RMS} reaches its apex value of ~200 nm at the highest irradiation fluence of 1.75 J/cm^2. This is an order of magnitude larger compared to the roughness of the non-irradiated surface (*i.e.* ~20 nm) and surface irradiated at 0.44 J/cm^2 (*i.e.* ~35 nm). Additionally, the areas treated with higher laser fluence (1.75 J/cm^2) contain larger grains than the areas irradiated with lower laser fluence (0.44 J/cm^2) (Fig. 14 (b) vs. (c)). Consequently, higher R_{RMS} values are obtained in the case of 1.75 J/cm^2 irradiated surfaces with respect to those irradiated at 0.44 J/cm^2. A greater scan speed of 4 mm/s versus 0.5 mm/s results in a decreased number of pulses incident on the surface and consequently in a reduced surface roughness. This is more evident in the case of the higher laser fluence (1.75 J/cm^2), where the R_{RMS} drops to ~140 nm, than in the case of the lower laser fluence (0.44 J/cm^2), where a R_{RMS} value of ~30 nm was recorded.

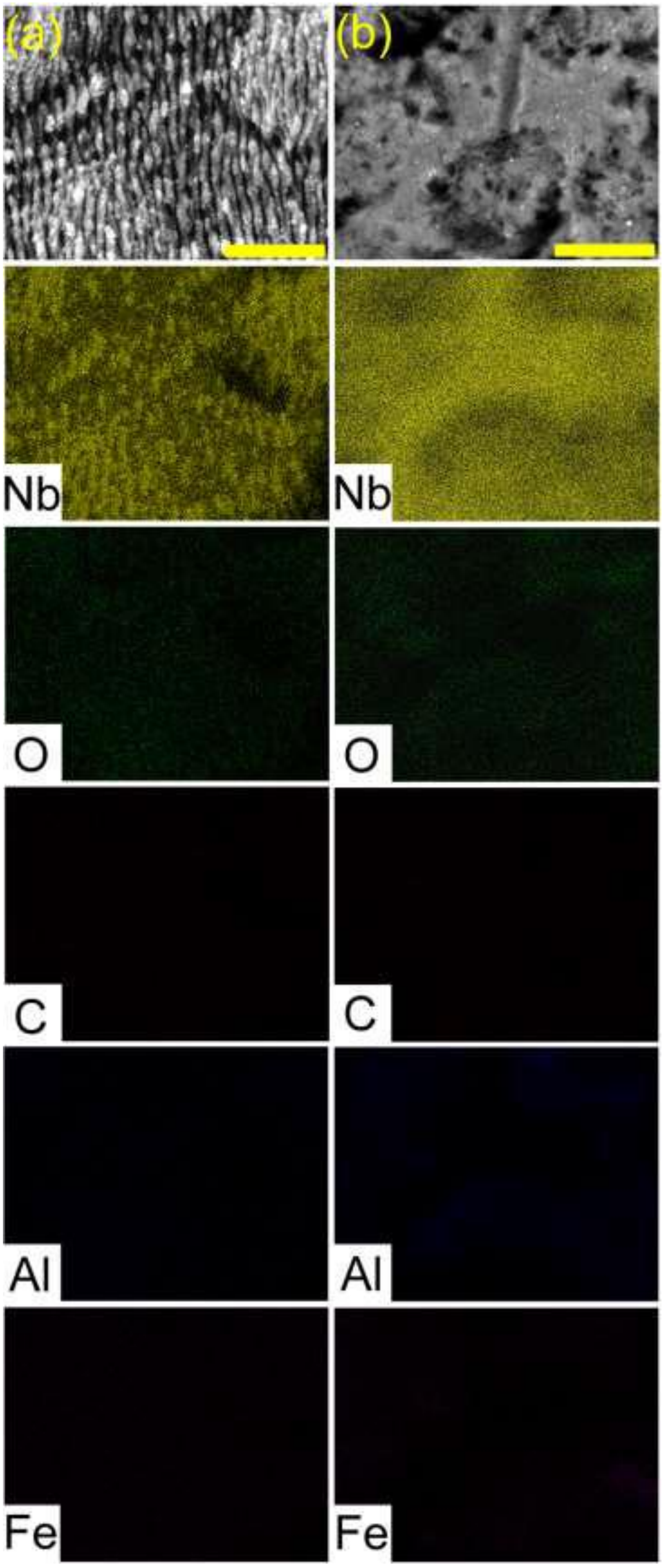

Fig. 13. EDS mappings and the corresponding SEM scanned fields (magnification bar=4 µm) of irradiated (a) and non-irradiated (b) areas of the sample treated with 1.75 J/cm^2 fluence laser pulses at 0.5 mm/s scanning velocity.

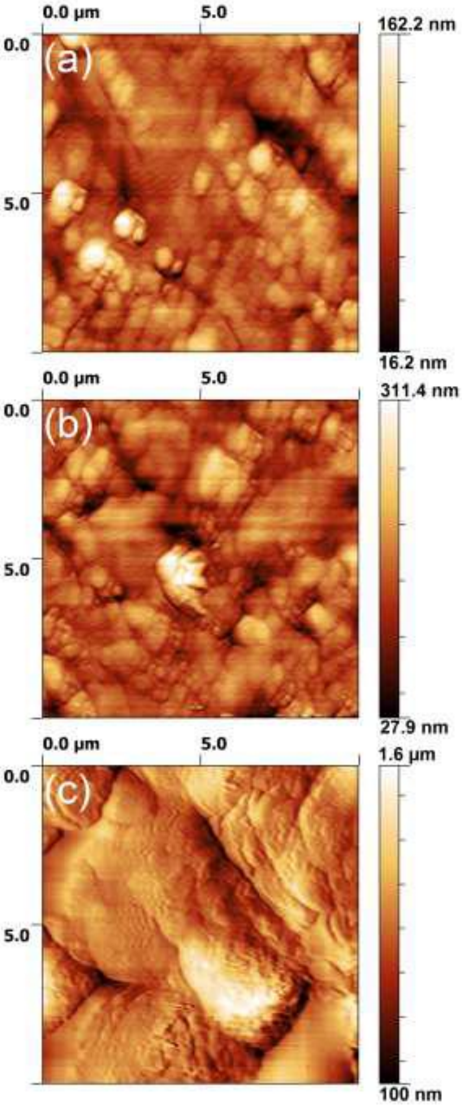

Fig. 14. Typical AFM images recorded on the reference disc (a) and discs laser treated at 0.44 J/cm^2 *irradiation fluence with 0.5 mm/s scanning velocity (b) and at 1.75 J/cm*^{2} *irradiation fluence with 0.5 mm/s scanning velocity (c)*

The typical GIXRD pattern of the Nb laser irradiated target is displayed in Fig. 15. The results should be viewed as global structural assessment of the sample. The reduced area of the irradiated regions impeded an individual local GIXRD investigation. Beside the prominent diffraction maxima of Nb (see Fig. 15(a)), one can notice the presence of shallow peaks which can be ascribed to impurities such as a rhombohedral Al_2O_3 phase (ICDD: 01-081-1667) or bcc iron phase (ICDD: 03-065-4899) (see Fig. 15 (b)). The starred peak located at $2\theta \approx 44.7°$ can be associated to the strongest intensity line of two other cubic phases: $Al_{0.5}Fe_3Si_{0.5}$ (ICDD: 00-045-1205) and/or $Fe_{0.905}Si_{0.095}$ (ICDD: 03-065-6323). The occurrence of such residual phases is in a good accordance with the EDS results (Fig. 12 and Table 3), which evidenced traces of Al, Fe and Si. We emphasize the presence of a hump in 2θ angular region 23–34°, which can be attributed to the formation of amorphous oxides, such as Nb_2O_5 or NbO_2 (with diffraction lines in this region).

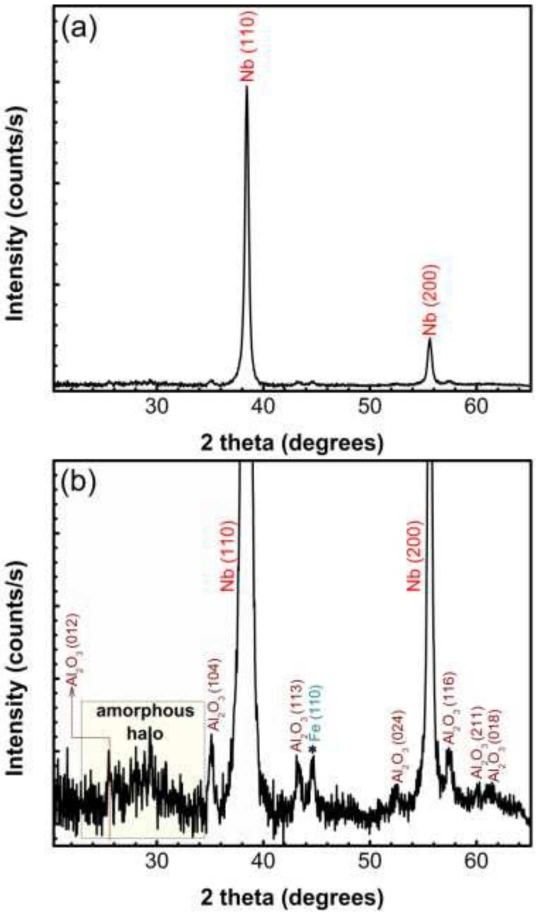

Fig. 15. Typical GIXRD pattern of Nb irradiated sample: general view (a) and zoomed view (b)

The typical morphology of the irradiated surface, as observed under the Raman optical microscope, is shown in Fig. 16. The islands of molten material, *e.g.* denoted as A and B on the photo, appear brighter with respect to the surrounding dark matrix (the rippled structure observed in the SEM image in Fig. 13a). Raman spectra taken from the metal-shining islands, as spot A in Fig. 16, revealed a strong Rayleigh background only with no distinctive Raman bands (results not shown). Thus, one may conclude that such regions correspond to a metallic, non- or poorly oxidized niobium (Fig. 13a). Spectra acquired from the less reflecting islands (*e.g.* spot B in Fig. 16) and from the surrounding dark material, displayed well-resolved Raman bands as visible from Fig. 17(a). The spectra from these regions can be divided into two well-separated parts: below and above 1000 cm^{-1}, respectively. The relative intensity of the low and high-frequency parts varies from island to island, and is related to the different chemical composition. The lines below 1000 cm^{-1} can be ascribed to a mixture of niobium oxides, whilst the two bands positioned at 1373 and 1403 cm^{1} originate from Nb-H vibrations in niobium hydrides. It is interesting also to note the wide background with a maximum at ~2400 cm^{-1} which could be absent or seen with variable intensity on different points of the irradiated areas. Its spectral position corresponds to a wavelength of ~725 nm and matches remarkably well the maximum of the photoluminescence (PL) signal found in hydrogenated amorphous carbon (a-C:H) materials. Based upon the abundance of carbon in our samples as evidenced by the EDS analyses (see Table 3) as well as the presence of Nb hydrides, one may hypothesize that the observed spectral band could be assigned to a-C:H which is formed as a result of the laser irradiation. That is why, hereafter, we will refer to the ~2400 cm^{-1} band as of a-C:H-PL band.

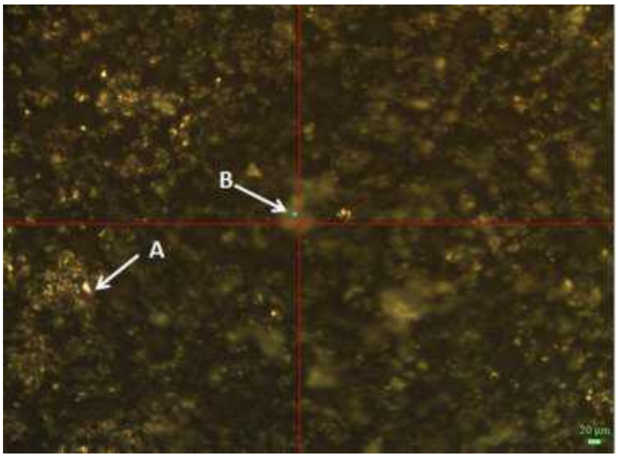

Fig. 16. Typical morphology of the Nb surface after irradiation with femtosecond laser pulses (1.75 J/cm^2 laser fluence, 0.5 mm/s scanning velocity) as observed under the Raman optical microscope. The shiny areas, like A, correspond to non- or poorly oxidized niobium. Less reflective areas, like B, display Raman features, characteristic of Nb oxides and hydrides. The spot near the crosshair indicates the laser focus during Raman measurements

After cleaning the Nb surface in ethanol, in order to remove contaminations, extremely strong and narrow Raman bands have arisen on specific islands. These additional strong spectral lines are superimposed to the spectrum of oxidized islands, as visible in Fig. 17(b). The spectrum is representative for the zone treated with 1.75 J/cm^2 laser pulses at 0.5 mm/s scanning velocity.

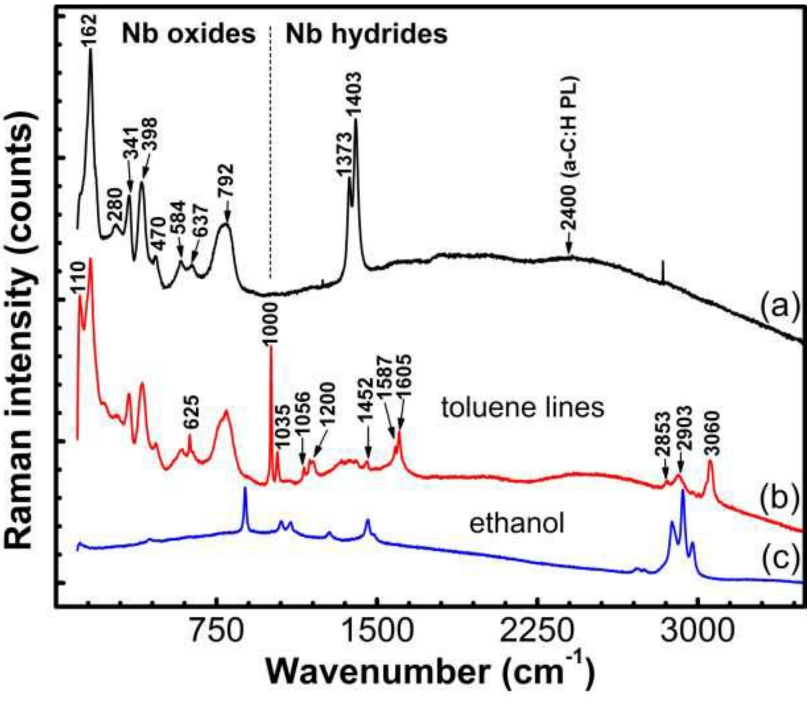

Fig. 17. (a) Raman spectrum taken from the island, denoted as B on Fig. 6. Marked lines are tentatively ascribed to Nb oxides and Nb hydrides. (b) Raman spectrum from the islands on the irradiated Nb surface after washing the samples in ethanol. The emerging toluene lines are labeled. (c) Reference Raman spectrum taken from the bulk of ethanol at the same laser power

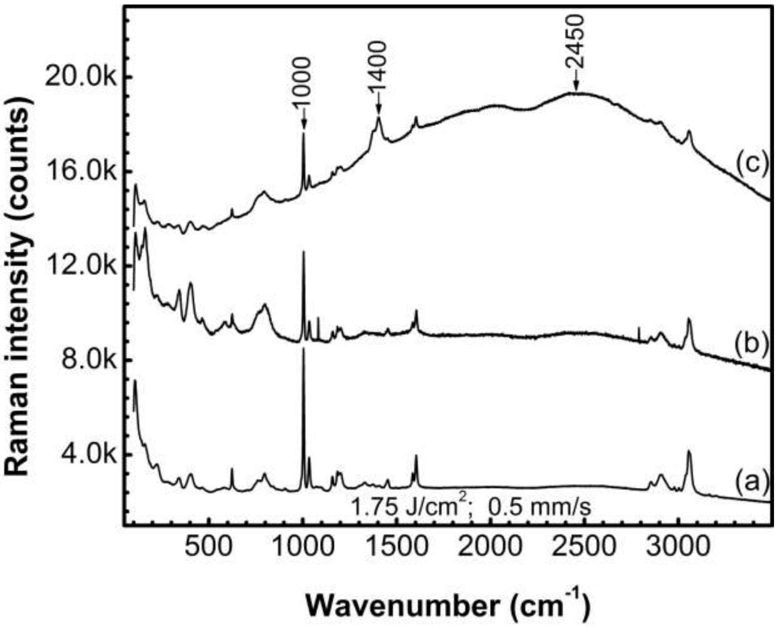

Fig. 18. Toluene SERS spectra superposed with different spectral features: (a) Nb oxides bands only (below 1000 cm^{-1}); (b) oxides and a-C:H-PL band (~2400 cm^{-1}); (c) oxides, a-C:H-PL and Nb hydrides (1400 cm^{-1}) bands

In Fig. 18 we present typical toluene spectra recorded on the area treated with a laser fluence of 1.75 J/cm^2 at a scanning speed of 0.5 mm/s. In the spectrum (a) the toluene lines are superposed with the Nb-oxides lines only. In spectra (b) and (c) the toluene lines overlay a-C:H-PL bands of different intensity, but are still well resolved. Additionally, in spectrum (c) the Nb-hydride lines around 1400 cm^{-1} are also present.

Toluene is a common trace additive in ethanol. Its concentration in our case is below the detection limit of the spectrometer, as demonstrated by the reference ethanol spectrum taken at the same laser power irradiation (see Fig. 17(c)). The relative intensity of toluene lines is maximal on the top of the islands and gradually decreases towards periphery. One may therefore assume that the islands on the Nb surface act as hot spots for toluene molecules leading to a boosted SERS effect, while the rippled structure of the surrounding dark material does not contribute significantly to enhanced scattering. The concentration of hot spots and the toluene bands intensity scaled approximately with the roughness of the irradiated surface, reaching its maximum for the areas treated with 1.75 J/cm^2 laser pulses at 0.5 mm/s scanning speed. So far, no specific dependence of the toluene bands intensity on the molten island aggregation has been traced, many of the hot spots being located on isolated islands. Randomly chosen hot spots have been repeatedly tested in course of several days, while the samples have been stored at normal atmospheric conditions, and the toluene bands displayed full reproducibility.

The as defined SERS estimator and its relative standard deviation over an ensemble of 20 hot spots are plotted in Fig. 19 against RMS surface roughness (R_{RMS}) for the areas treated at the scanning speed of 0.5 mm/s and laser fluences varying between 0.44 and 1.75 J/cm^2. The graph in Fig. 19(a) clearly shows the trend of increasing of SERS enhancement with the surface roughness. This tendency is also illustrated in Fig. 20, where series of toluene SERS spectra taken on areas of increasing roughness (from (a) to (c)) are shown. As evidenced from Fig. 19(b), the relative standard deviation of SERS enhancement drops from 51% to 20% upon increasing of R_{RMS}.

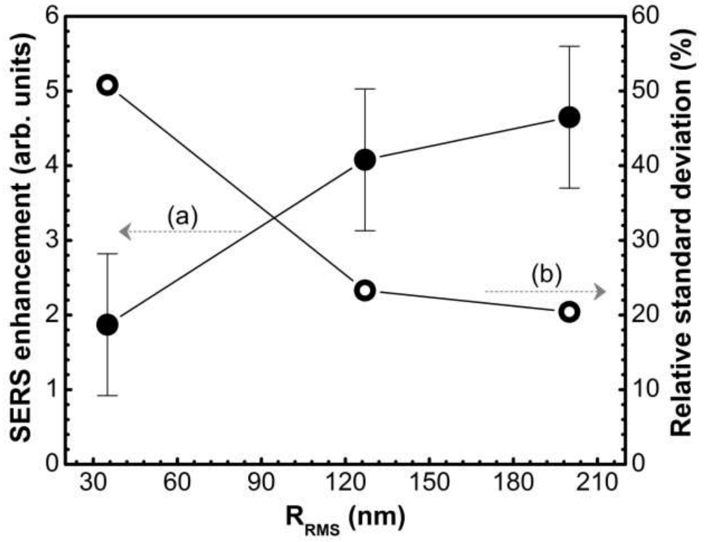

Fig.19. ((a) Normalized SERS enhancement for the toluene line at 1000 cm^{-1} averaged over areas of different roughness (R_{RMS}), treated with laser fluence ranging from 0.44 to 1.75 J/cm^2 at a scanning speed of 0.5 mm/s. Error bars indicate the absolute standard deviation of the SERS enhancement. (b) The relative standard deviation of the SERS enhancement versus surface roughness

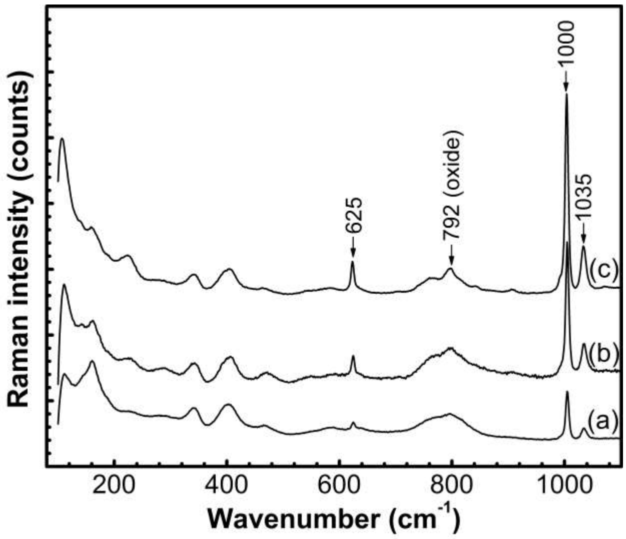

Fig. 20. Comparison between intensities of the strongest toluene line at 1000 cm^{-1} and the Nb oxides bands for areas of different roughness treated with different laser fluence, as follows: (a) 0.44 J/cm^2, R_{RMS} = 35 nm; (b) 1.33 J/cm^2, R_{RMS} = 130 nm; (c) 1.75 J/cm^2, R_{RMS} = 200 nm

We tested the SERS activity of the irradiated Nb surface with respect to rhodamine 6G (R6G) molecules which is a common analytic test for SERS substrates. A reference spectrum of 10^{-3} M water solution of R6G is shown in Fig. 21(a). R6G was diluted to a concentration of 10^{-5} M and the Nb sample was immersed into solution. The Raman spectrum of the immersed sample is given in Fig. 21(b). Again, the spectrum is characteristic to the zone treated with 1.75 J/cm^2 laser pulses at 0.5 mm/s scanning velocity.

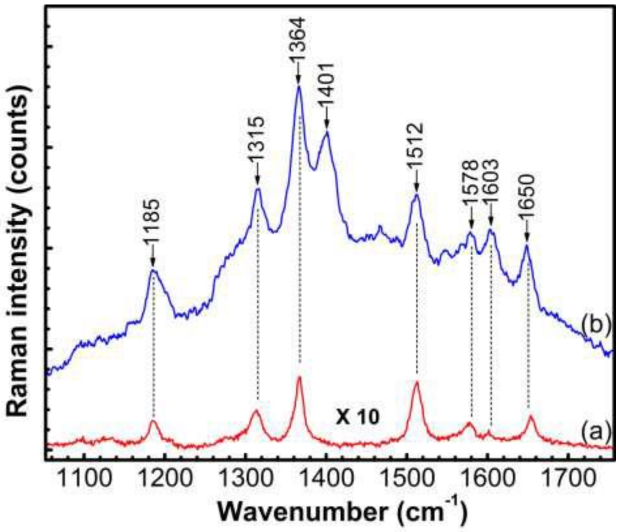

Fig. 21. (a) Raman spectrum from the bulk of 10^{-3} M water solution of R6G. (b) Raman spectrum taken from the islands on the irradiated Nb surface in the 10^{-5} M R6G solution. Both spectra are taken at the same laser power and acquisition time. Spectrum (a) is multiplied by a factor of 10 for clarity

As evidenced by the two-dimensional (2D) Raman scan in Fig. 22, R6G Raman lines are clearly detectable on the islands, with intensity surpassing by more than an order of magnitude the Raman signal collected on the surrounding material. The extra line at 1401 cm^{-1} originates from the Nb–H bonds vibrations (see Fig. 17(b)). Based upon the comparative spectra in Fig. 21, one can estimate an average SERS enhancement factor of ~1.3×10^3 for R6G.

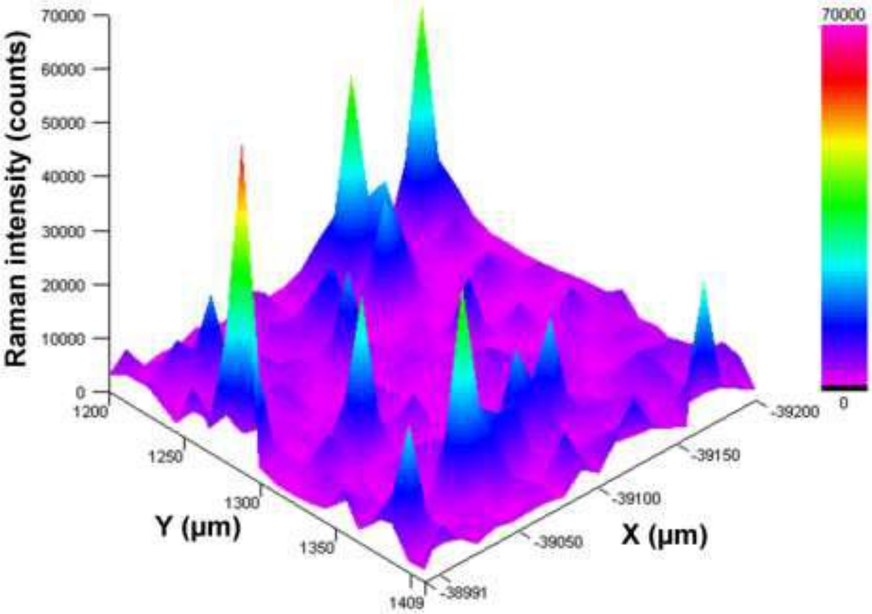

Fig. 22. Two-dimensional Raman scan of the intensity of the strongest R6G line at 1364 cm^{-1} on a 200 μm × 200 μm surface treated with a laser fluence of 1.75 J/cm^2 at a scanning speed of 0.5 mm/s. The units on vertical axis are photon counts. The area is scanned over a mesh of 20 × 20 points separated by a distance of 10 μm. The sharp intensity maxima coincide with the positions of elevated molten islands

The SERS properties of Nb surfaces after irradiation with femtosecond laser pulses were demonstrated. We were able to detect traces of toluene diluted in ethanol, as an effect of samples' surface immersed in ethanol. It was shown that the SERS enhancement of toluene Raman lines and its reproducibility among different hot spots increase with surface roughness. The estimated detection limit for toluene is competitive to those reported for silver-based plasmonic structures. Further, SERS effect has been investigated for R6G solutions, and an enhancement factor of order of 10^3 has been attested. Measurements showed that the islands of molten material serve as SERS hot spots, while the surrounding rippled structures do not contribute significantly to the enhancement of Raman signal.

Our findings point toward the potential of Nb as a good SERS alternative substrate material. To the difference of other alternative plasmonic metals, like copper, where surface oxides hamper the Raman enhancement, we observed that a good quality SERS signal is obtained even on oxidized Nb surface. Laser treated Nb substrates could be advantageous in sensing applications where mechanical robustness of the surface is essential, whilst the traditional plasmonic structures based on deposition of Au or Ag thin layers or nanoparticles are of limited mechanical stability.

3. "Pulsed Laser Deposition method for fabrication of CdS/TiO$_2$ and PbS photoelectrodes for solar energy application", Andjelika Bjelajac, Veljko Djokic, Rada Petrovic, George E. Stan, Gabriel Socol, Gianina Popescu-Pelin, Ion N. Mihailescud, Djordje Janackovic, Digest Journal of Nanomaterials and Biostructures 10 (2015), 1411-1418

This study aims to demonstrate the simplicity and feasibility of PLD method for sensitization of TiO$_2$ nanotubes with CdS as well as its use for fabrication of PbS counter electrode. The main goal of this work was studying the effect of the number of applied laser pulses on the structural properties of the photoanodes and their influence on the *I-V* characteristics of the assembled cell.

Fig. 23 displays a typical top-view SEM micrograph of an as-sputtered titanium film. The SEM analyses revealed well-adhered films with a homogeneous nanostructured surface, consisting of merged nanograins, having the average diameter of ~200 nm. No signs of either microcracks or delaminations were noticed. Fig. 23-inset presents the cross-view SEM image of the titanium film. One can observe that the ~1.6 μm thick film has a columnar structure, typical for radio-frequency magnetron sputtering (RF-MS) films grown at room temperature.

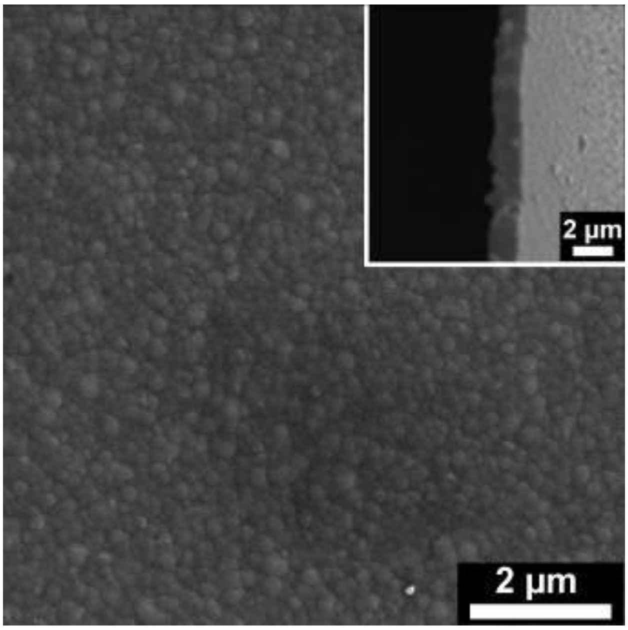

Fig. 23: Typical SEM surface and cross-sectional morphology (inset) of as-sputtered titanium films

Fig. 24 shows FESEM micrographs of the surface microstructure of Ti film coated on the FTO glass substrate after the anodization, revealing the 3.5 μm long TiO$_2$ nanotubes with a ~60 nm inner diameter. Compared to the thickness of the Ti film (~1.6 μm) the length of the nanotubes is increased due to the high porosity of TiO$_2$ film. The transparency of the obtained TiO$_2$ films is indicative for the Ti amount consumed in formation of TiO$_2$ layer.

In a previous study, we showed that 250 and 500 laser pulses were sufficient to sensitize ~100 nm wide nanotubes. Therefore, herein for narrower pores structure the number of the laser pulses was set to 200 and lower.

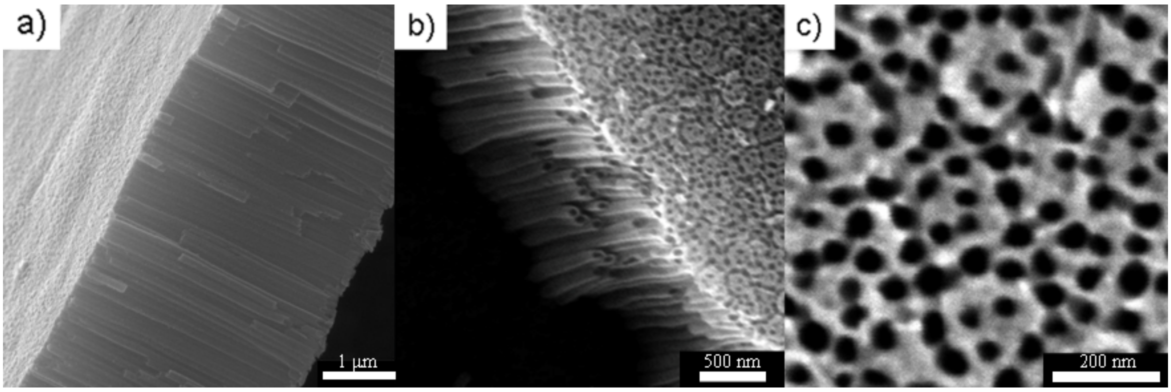

Fig. 24. SEM micrographs of as-prepared TiO2 nanotubes: (a) cross-view image showing the nanotubes length of 3.5 μm; (b) tilt-view image presenting more clearly the TiO2 nanotubes' structure; and (c) top-view imagine highlighting the inner diameter (~60 nm) of the nanotubes

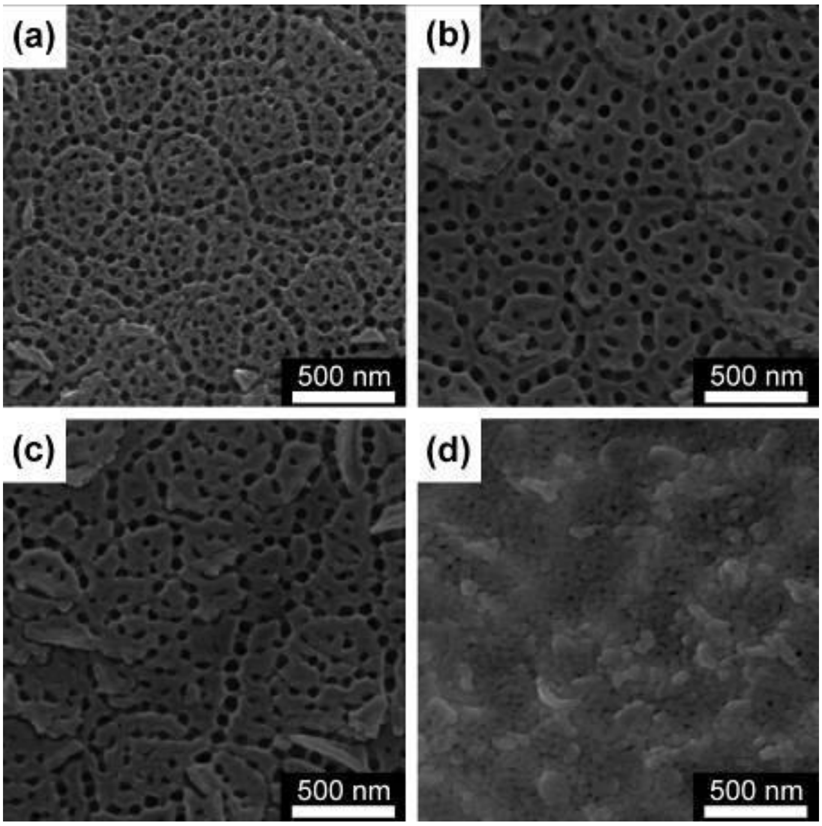

Fig. 25: Typical FESEM images of the: (a) NT50, (b) NT100, (c) NT150 and (d) NT200 samples

Fig. 25 gives the overview of the FESEM images of the TiO_2 nanotubes after the CdS deposition, corresponding to different number of pulses. For the samples NT50, NT100 and NT150 on can notice that the nanotubular structure remains open without clogging, which ensures the electrolyte penetration for further assembly of the cells. However, in the case of the NT200 samples the excess of CdS is noticed, which now obturates the TiO_2 nanotubes, whose typical morphology is hard to discriminate. Such situation should be avoided since it can cause the increase of the recombination of the electron-hole pairs. By decreasing the distance that charge carriers should cross inside the sensitization layer to reach the electrolyte or the underlying TiO_2, the recombination of the electron-hole pairs can reach a minimum. Therefore, the sample NT200 was excluded from the further investigations. By comparing Fig. 25 to Fig. 24, a certain narrowing of the nanotubes diameter can be observed as a consequence of CdS coverage by PLD. From the FESEM micrographs (Fig. 3) the inner diameter was estimated as: a) ~55 nm (NT50), (b) ~50 nm (NT100) and c) ~45 nm (NT150).

The results of EDS study of NT50, NT100 and NT150 samples, are collected in Table 4. It is obvious that the amount of CdS deposit increases with the number of laser pulses applied for deposition. One notes that Si and Sn signals originate from FTO substrates.

Table 4: Chemical composition (at. %) of NT50, NT100 and NT150 samples, inferred by EDS analysis

Element	Sample		
	NT50	NT100	NT150
O	74.25 ± 0.29	73.16 ± 0.24	72.59 ± 0.23
Si	0.08 ± 0.02	0.11 ± 0.02	0.08 ± 0.02
S	0.10 ± 0.04	0.15 ± 0.02	0.31 ± 0.02
Ti	25.33 ± 0.27	26.27 ± 0.24	26.60 ± 0.23
Cd	0.10 ± 0.02	0.16 ± 0.03	0.27 ± 0.03
Sn	0.12 ± 0.01	0.14 ± 0.02	0.15 ± 0.03

The GIXRD analysis (Fig.26) of the obtained CdS/NT150/FTO photoanodes showed clearly that TiO_2 nanotubes had a majoritary anatase structure (ICDD: 00-021-1272). Traces of a titanium sub-oxide phase (Ti_6O – ICDD: 01-072-1471) have been also evidenced. The diffraction peaks of CdS deposits were difficult to emphasize due to the low amount of CdS and the partial overlapping of its diffraction lines on the prominent diffracted signals originating from the anatase nanotubes arrays and the bottom FTO conductive substrate (ICDD: 01-077-0452). In order to tackle this problem, and assess the nature of the PLD deposits, GIXRD investigations have been performed on CdS structures deposited under the same working conditions onto bare silica glass substrates. This way by performing overnight measurements it was allowed the detection of CdS phase, but only for the sample prepared by applying a higher number (150) of laser pulses. The GIXRD patterns of NT100 and NT150 are presented comparatively in Fig. 26-inset. One can observe the broaden diffraction peaks (characteristic of a nanosized material) corresponding to a hexagonal CdS phase (ICDD: 01-080-0006), superimposed on the amorphous halo assigned to the silicate glass structure. A *c*-axis preferential orientation of CdS deposit, in the case of NT150, is suggested by the increase of the 002 line intensity with respect to the reference diffraction file (ICDD: 01-080-0006), and the strong diminution of the highest intensity line (101) of the hexagonal CdS phase. No diffraction maxima could be emphasized in the case of NT100 sample, measured in identical conditions (Fig. 26-inset), due to the reduced amount of pulsed laser deposited CdS material, situated under the sensitivity limit of the XRD machine employed in this study.

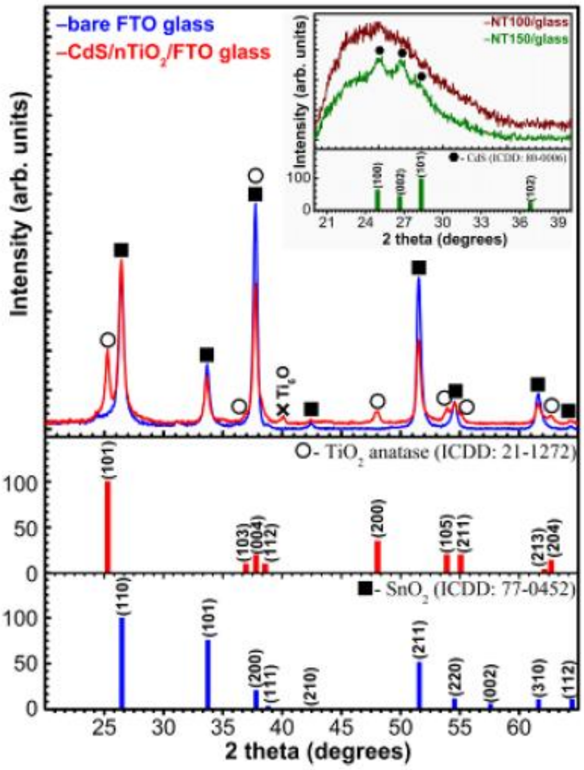

Fig. 26: Typical XRD pattern of CdS/NT150/FTO photoanode. Inset: XRD diagrams of CdS structures deposited onto bare glass substrate by applying 100 and 150 laser pulses. The ICDD reference files of TiO_2-anatase, SnO_2 and CdS are also inserted for comparison

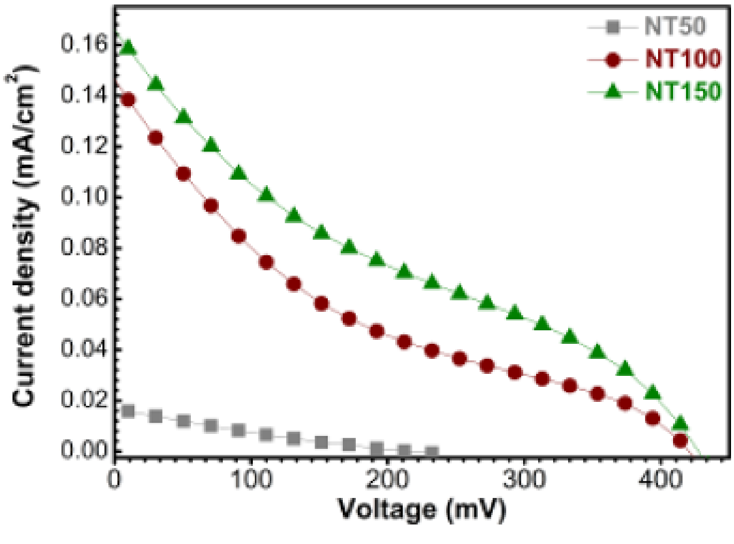

Fig. 27: I-V characteristics of the photovoltaic cells with NT50, NT100 and NT150 photoanodes

After injecting the electrolyte between the assembled electrodes, the cells *I*-*V* performance parameters were measured both in dark and illumination with simulated sunlight at 1.5 AM (100 mW/cm^2). All solar cells evidenced the photovoltaic effect as visible from the graphs presented in Fig. 27. By comparing the graphs enclosed in Fig. 27, it is obvious that when the amount of the CdS deposit increases the current density and voltage increase. However the shape of the curves indicates the low value of the fill factors (~0.20) which can be attributed to the poor hole-recovery rate of polysulphide, leading to a high rate of surface recombination at the QD/electrolyte interface.

Our study emphasized the 150 laser pulses as the optimal value for the CdS deposition within the ~60 nm wide TiO_2 nanotubes arrays. At lower numbers of pulses the photovoltaic cell parameters decline, whilst at the higher number of pulses the nanotubes are clogged.

The pulsed laser deposition method was also used to obtain a PbS counter electrode. Its wide absorption range (300-700) nm is shown in Fig. 28 where the additional transmittance spectrum of CdS thin film is given for comparison. This result points to the advantage of use PbS as a counter electrode since it provides additional amount of excited electrons that TiO_2 photoanode was not able to absorb. PbS here serves therefore as a photocathode in this configuration of the solar cell.

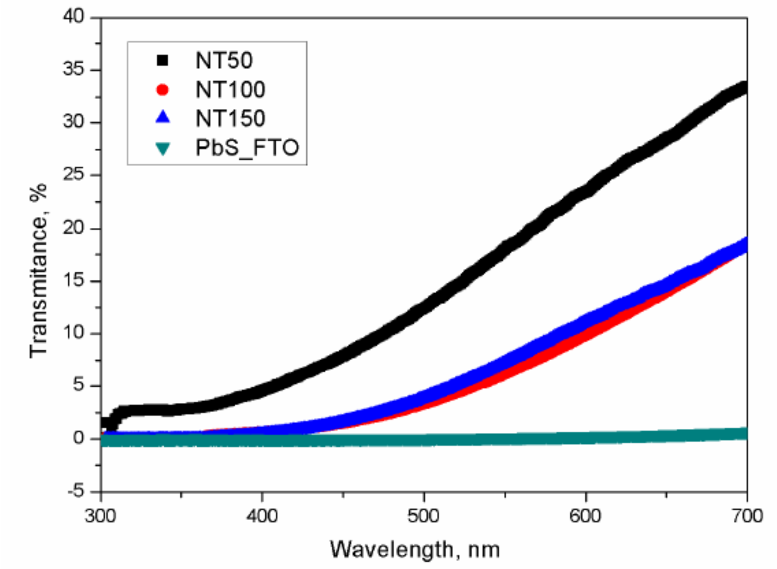

Fig. 28: UV-VIS transmission spectra of CdS versus PbS thin films within the (300-700) nm spectral range

We demonstrated that the pulsed laser deposition of CdS for sensitization of titania photoanode can be tailored by changing the number of laser pulses, suggesting that this less explored technique is a promising alternative for the CdS deposition. Under one-sun illumination, the *I-V* characteristics of the assembled solar cells were measured and the best photovoltaic performance has been obtained in the case of cells with TiO_2 nanotubes sensitized with CdS by applying 150 laser pulses.

A complete absorption of light within (300-700) nm spectrum was observed in case of PbS films playing an advantageous role as a photocathode.

4. ***“Matrix assisted pulsed laser deposited CdS quantum dots sensitized solar cells”***, A. Bjelajac, R. Petrovic, G. Socol, I. N. Mihailescu, M. Enculescu, V. Grumezescu, V. Pavlovic, Dj. Janackovic, submitted for publication in Applied Surface Science

CdS targets were prepared by freezing with liquid nitrogen the 2 ml volume of the corresponding CdS/DMSO dispersion. The UV laser source was a pulsed KrF* excimer laser operating at 248 nm, with a pulse duration of 25 ns. The beam was focused in a spot of 10 mm^2 onto the surface of the CdS target previously at the repetition rate of 3 Hz. The residual pressure inside chamber was 10^{-3} Pa and the targets were kept frozen during the irradiation. The substrate holder was placed parallel to the target at a 50 mm separation distance. During the laser deposition, the targets and the substrates were continuously rotated (30 rot/min) in order to avoid the piercing of the targets and to ensure the deposition uniformity.

This study showed that the size of the CdS nanoparticles synthesized in DMSO can be controlled with microwave treatment that causes the release of S^{2-} ions from DMSO for creation of CdS nuclei and/or their further growth. The optimization of CdS synthesis is achieved by varying the duration of the microwave treatment and the microwave power.

The absorption spectra of CdS colloids synthesized in DMSO with and without microwaves radiation are shown in Fig. 29. For the both colloids a blue shift of absorption onset in comparison to bulk material, λ_g = 517 nm, indicated that CdS particles are in the quantum confinement regime. The absorption onset of Pre MW treated colloid was set at λ_g = 412 nm (curve b)), whereas for No MW colloid the absorption onset was set at λ_g = 400 nm (curve a)). The effective mass approximation model (EMM) was used to estimate the size of CdS nanoparticles from the increase of the band gap energy. Taking into account the band gap energy of E_g = 3.10 eV that corresponds to the experimentally determined absorption onset for No MW colloid and E_g = 3.01 eV for Pre MW colloid, and known values for effective masses of electrons and holes (m_e = 0.19 m, m_h = 0.8 m, where m is the free-electron mass), the size of CdS QDs was found to be 3.16 nm and 3.35 nm, respectively.

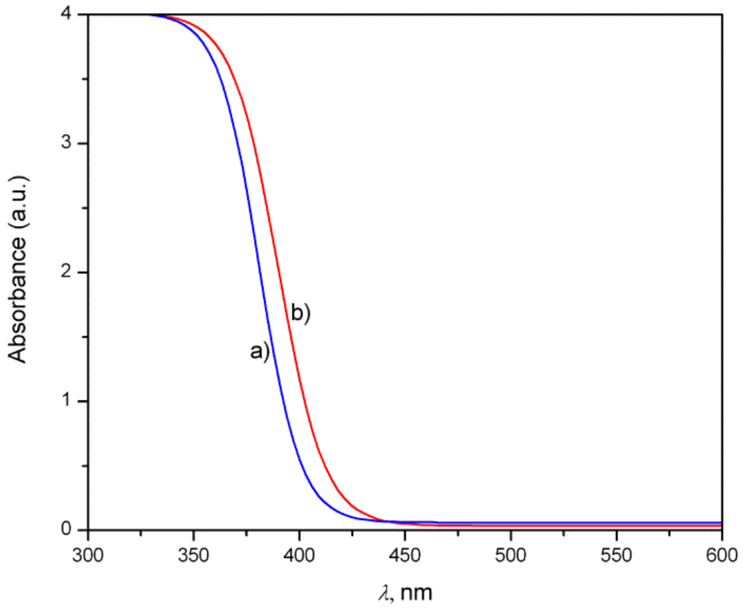

Fig. 29. Absorption spectra of: a) No MW CdS/DMSO colloid and b) Pre MW CdS/DMSO colloid

These results indicate that MW treatment influenced the size of the CdS nanoparticles. Due to the MW radiation that converts into heat S^{2-} ions are released from DMSO and they react with dissolved Cd^{2+} ions forming CdS nuclei that further growth by adding S^{2-} ions dissolved in DMSO. Since, the same concentrations of Cd_{2+} and S_{2-} are used for preparation of No MW and Pre MW treated sols the difference in size of CdS particles can only be due to the MW radiation.

In order to verify the estimation of CdS QDs size, the TEM analysis was performed and the results are summarized in Fig. 30. No significant difference between the two colloids can be observed. The size of the detected nanoparticles is in the range of 2-4 nm, which is in accordance with the calculated values using EMM.

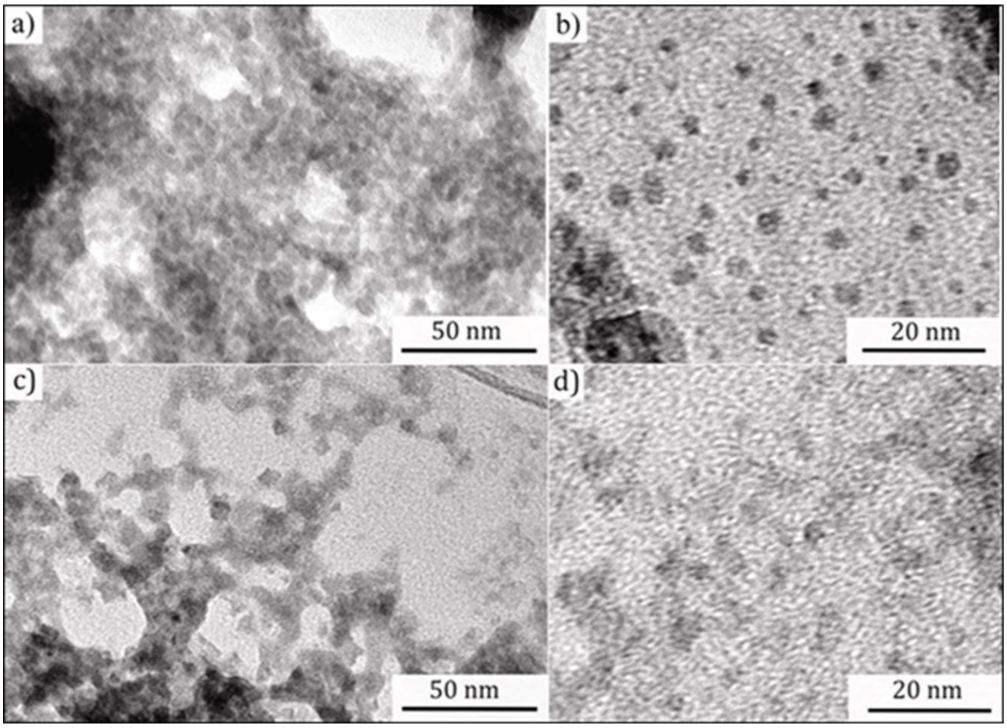

Fig. 30 TEM micrographs of: a) and b) No MW CdS colloid, c) and d) Pre MW treated CdS colloid

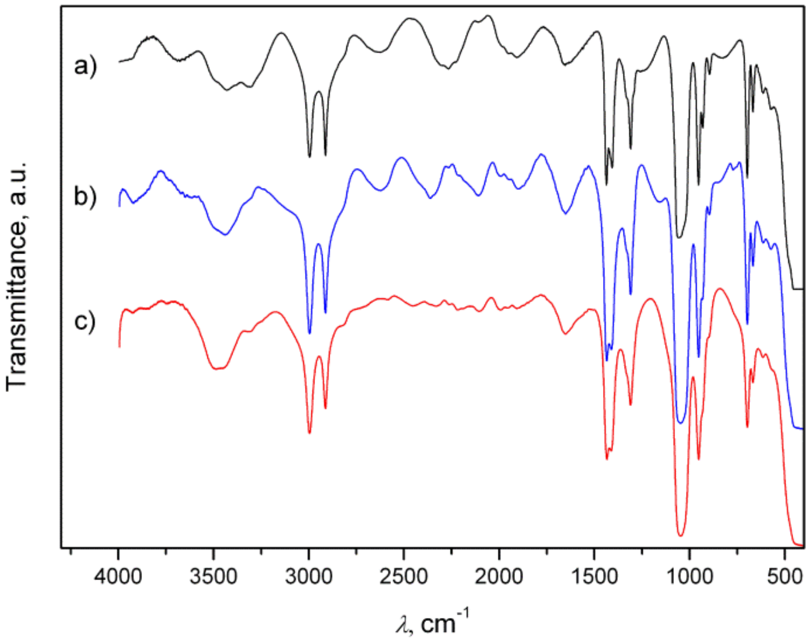

Fig. 31. FTIR spectra of: a) pure DMSO, b) No MW CdS/DMSO colloid and c) Pre MW treated CdS/DMSO colloid

The discernment of the molecular structure of the synthesized colloids was obtained by FTIR analysis. The spectra of CdS colloids are presented in Fig. 31 together with the FTIR spectrum of pure DMSO for comparison. The predominant peaks for DMSO at 614, 668, 698 cm^{-1} attributed to CSC bonding, 896, 954, 1310, 1408, 1437, 2913, 2996, 3305 and 3432 cm^{-1} for CH_3 vibrations and the most intensive peak at 1058 cm^{-1} associated to SO stretching vibrations are also detected for CdS/DMSO colloids. The noticeable difference can be observed in the frequency region 1550-2750 cm^{-1}, 1100-1280 cm^{-1} as well as in 725-880 cm^{-1}. Also, the DMSO peaks at 2267 cm$_{-1}$ and 3688 cm^{-1} do not appear for CdS colloids. In the case of No MW colloid the peaks at 2111 and 2362 cm^{-1} are more intensive than for the Pre MW treated colloid. Furthermore, the peaks at 770 and 1160 cm^{-1} are detected for No MW colloid but not for Pre MW treated colloid, which could be a consequence of a Cd(S)-DMSO complex formation at the surface of CdS.

Fig. 32 presents the FESEM micrographs of the annealed TiO_2 nanotubes, since it is already shown that the annealing in air at 450 °C does not affect the nanotubular morphology. FESEM analysis showed that the obtained films have homogeneous structure with highly ordered pores (Fig. 32a)). The films consist of the ~ 3 μm long nanotubes (Fig. 32b)) with the inner pore diameter ~60-70 nm (Fig. 32d)).

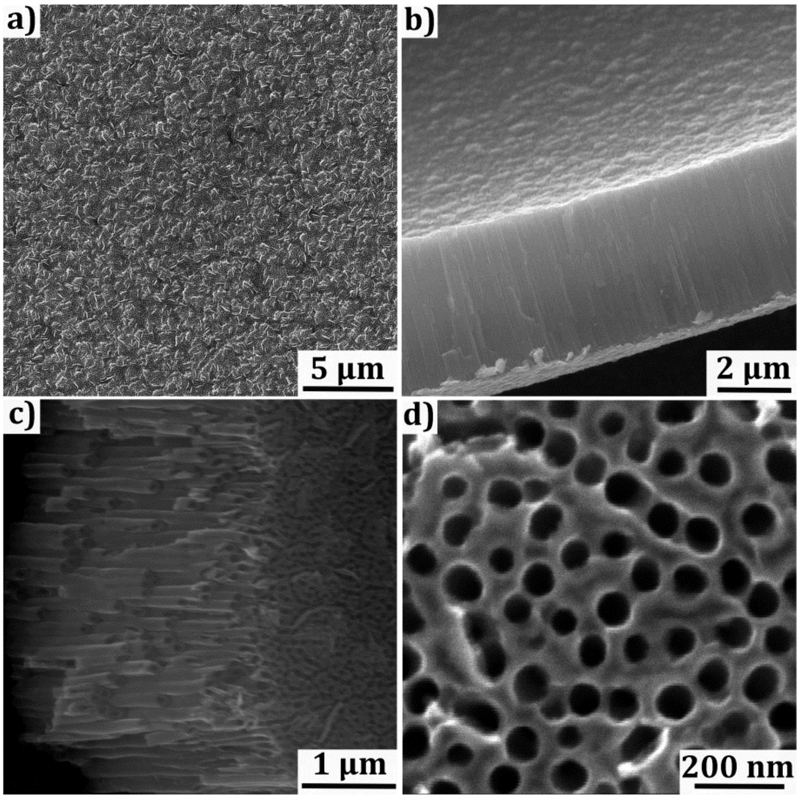

Fig. 32. FESEM micrographs of the annealed TiO2 films: a) the top view for the presentation of homogeneous structure of highly ordered pores, b) side view to show the nanotubes length of ~ 3 μm, c) angular view of higher magnification to present the structure more clearly and d) top view for estimation of the nanotubes inner diameter of ~ 60-70 nm

Fig. 33 gives an overview of the results of FESEM analysis of TiO_2 nanotubes after MAPLE deposition of CdS quantum dots using No MW and Pre MW treated CdS/DSMO sols as targets. A slight change in films morphology can be noticed regards to the decrease of the inner diameter of the nanotubes comparing to the Fig. 32, which is an evidence of the deposition.

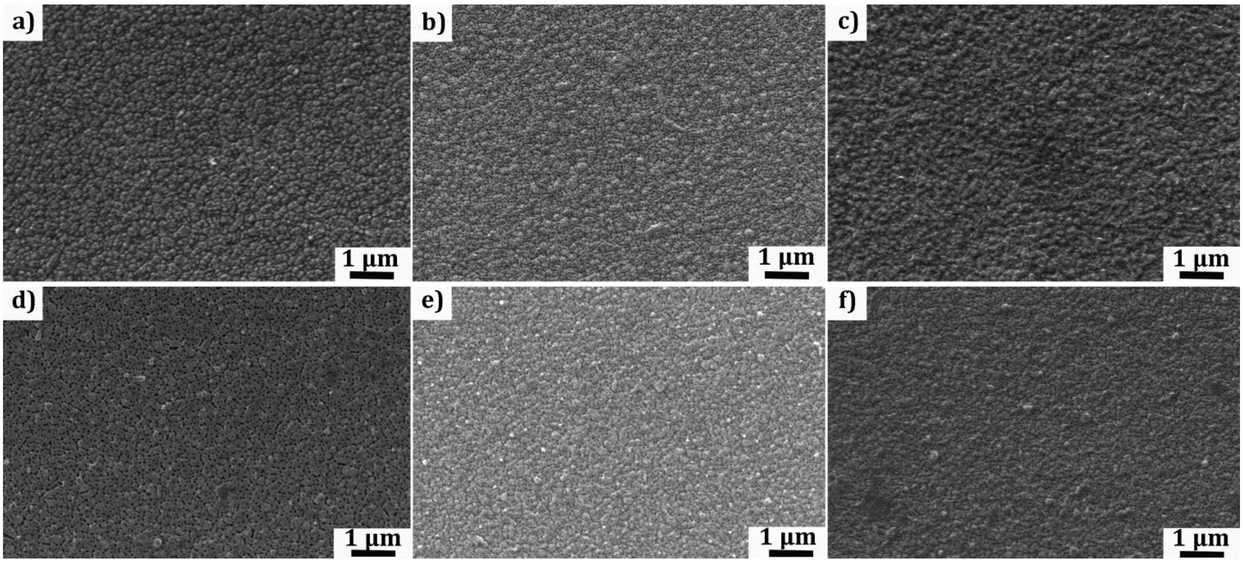

Fig. 33. FESEM overview of TiO2 nanotubes after MAPLE deposition of CdS using No MW sol as a target and applying: a) 2000, b) 2500 and c) 3000 laser pulses; and using Pre MW treated CdS target applying: d) 2000, e) 2500 and f) 3000 laser pulses

The EDS technique was employed for chemical structure analysis of the obtained samples. Table 5 summarizes the EDS results for pure TiO_2 film onto FTO glass and TiO_2 films with CdS deposit obtained by applying 2000, 2500 and 3000 laser pulses using No MW and Pre MW sols as targets for MAPLE. After the deposition the presence of Cd and S is obvious from Table 5 where their highest amounts are detected for the sample obtained using Pre MW treated sol with 3000 laser pulses.

Table 5: Chemical compositions (at.%) of all samples obtained via EDS analysis

Element	Pure TiO_2	TiO_2/CdS No MW-2000	TiO_2/CdS No MW-2500	TiO_2/CdS No MW-3000	TiO_2/CdS Pre MW-2000	TiO_2/CdS Pre MW-2500	TiO_2/CdS Pre MW-3000
O	75,95	70,36	70,26	72,2	59,01	55,01	51,56
Si	10,95	8,10	10,31	12,72	7,88	12,55	12,32
Ti	2,28	8,46	5,52	0,48	15,91	11,08	13,08
Sn	10,81	12,58	13,32	14,15	16,95	19,95	21,34
Cd	/	0,25	0,27	0,33	0,15	0,33	0,76
S	/	0,20	0,23	0,26	0,10	0,34	0,94

Solar cells are assembled with corresponding CdS/TiO_2 photoanodes and PbS cathodes where the liquid electrolyte was injected between. Fig. 34 shows the *I-V* curves resulting by measuring the current density under AM1.5 solar simulated illumination for the solar cells with CdS/TiO_2 photoanodes obtained using No MW CdS target applying: a) 2000, b) 2500 and c) 3000 laser pulses, whereas Fig. 35 presents the *I*-V curves of the cells obtained using Pre MW treated CdS sols applying: a) 2000, b) 2500 and c) 3000 laser pulses. Comapring the diagrams form Fig. 34 and Fig. 35 it can be notices that the cells obtained using Pre MW treated CdS sols show higher current densities and open circuit voltages, which can be explained due to the presence of Cd(S)-DMSO complex on the surface of CdS nanoparticles within Pre MW treated colloid. The Cd(S)-DMSO complex enhances the linkage between CdS quantum dots and TiO_2 nanotubes providing better electron transfer and I-V characteristics. In the case of solar cells obtained using No MW CdS colloid the maximum current density was measured to be 0.016 mA/cm^2, whereas in the case of using Pre MW colloid the maximum current density is 0.042 mA/cm^2, both for the 3000 laser pulses applied in MAPLE.

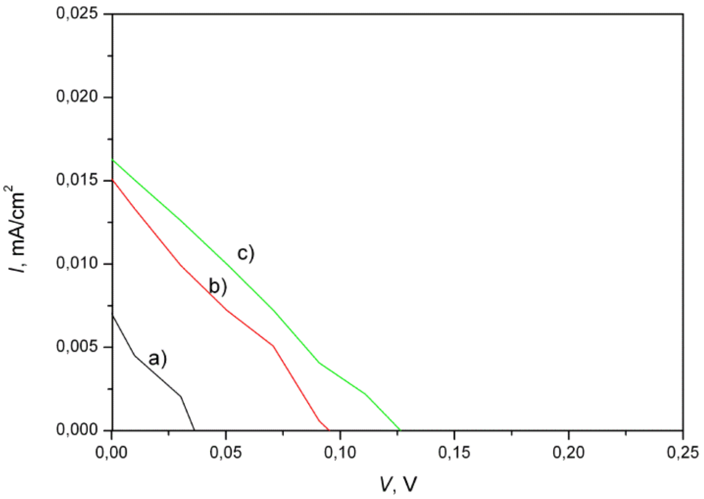

Fig. 34. I-V curves for solar cells with CdS/TiO2 photoanodes obtained MAPLE deposition technique using No MW target applying: a) 2000, b) 2500 and c) 3000 laser pulses

By comparing the diagrams according to the number of applied laser pulses, in both cases (No MW and Pre MW targets) the highest values of current density and voltage are observed for the cells whose CdS targets sustained 3000 laser pulses, thus for the highest amount of detected CdS using EDS technique.

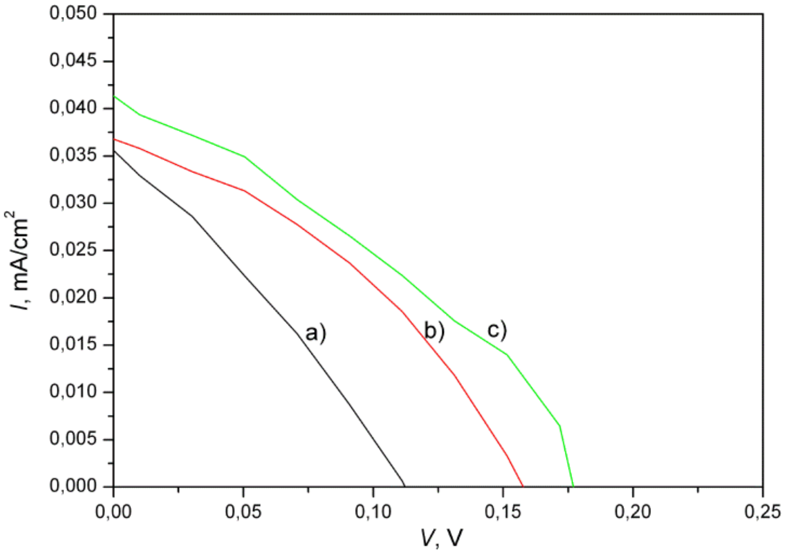

Fig. 35. I-V curves for solar cells with CdS/TiO2 photoanodes obtained MAPLE deposition technique using Pre MW target applying: a) 2000, b) 2500 and c) 3000 laser pulses

Better PV performance of the cells obtained with the use of microwave treated CdS sol can be due to the presence of Cd(S)-DMSO complex on the surface of CdS particles that improves the linkage between CdS and TiO_2 providing the enhanced electron transfer and consequently better PV performance.

Description of the technological update of the installation for sensors characterization designed and assembled in the "Laser-Surface-Plasma Interactions" Laboratory, INFLPR, with financial contribution of UEFISCDI under the contract ID 304/2011

Due to the fact that the gas sensing system is in the testing stage, the gases used for tests during this time were not CO, CO_2, O_2, N_2 and NO_2 (for which the MFCs are designed to work), some of them being hazardous for human, but compressed air was used instead. For this purpose the MFCs inlet was connected through small diameter plastic pipes to the laboratory compressed air supply outlet. The air circulation through the MFCs at well established flow rates was tested using the C960 Gas Mixing software and it was successful for the four Alicat MFCs as well as for the Aalborg MFC. The next step will be to connect the outlets of the MFCs to the inlet of the gas chamber where the sensor will be placed for the sensititvity study.

Regarding the LabView software in the form which was built until now this one means to detect the messages exchanged between the computer and MFCs the messages containing information about the MFC toward which the message is sent and is identified by the capital letters A, B, C, D (for Alicat) and F(for Aalborg), the mass flow rate which is a real number and the time at which the message was sent in the format hh:min:sec. At this project stage a further improvement of the LabView software was done with the purpose to improve the quality and the precision of the measurement done on the gas sensor.

As it was presented in the last phase the gas sensor is tested to detect the change in its electrical resistance which in turn gives information about gas mixture composition qualitative as well as quantitative. Regarding this purpose it is to mention that the gas sensor electrical resistance measurement must be realized after a time for the gas flow in the chamber to become laminar i.e. this one must reach a homogenous and stationary phase.

For this purpose the LabView software was modified and as a new thing the possibility of setting a delay time was introduced for the user. The delay time is setting the moment when the gas sensor electrical resistance measurement will start after the gas flow in the MFCs reached the nominal value set and the computer finished exchanging information with them.

In Fig. 36 the block diagram for the LabView software designed to introduce a delay time in the measurement of the sensor electrical resistance is given.

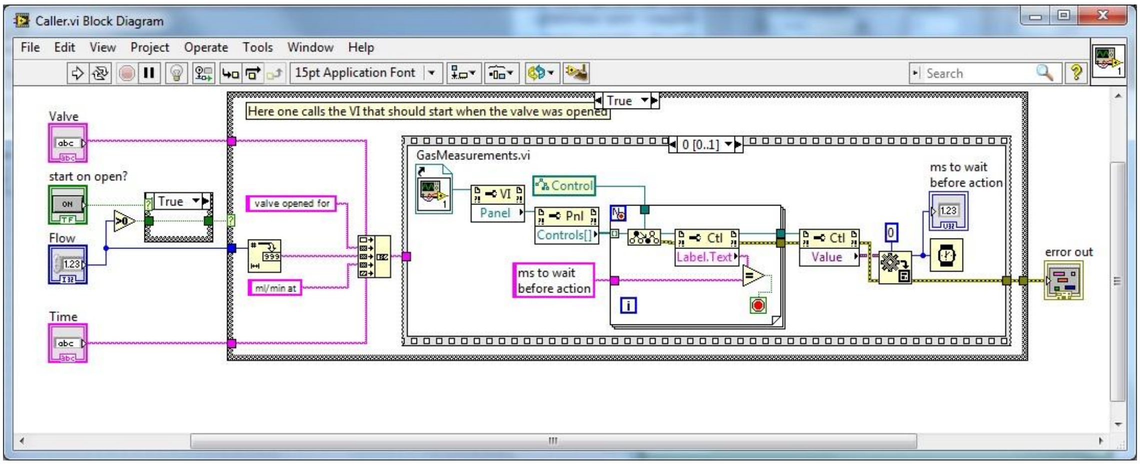

Fig.36. The modification introduced in the Caller.vi block diagram which allows the setting of a delay time in the electrical measurement of the gas sensor

Other contributions with acknowledgements to this contract, which were not presented in this report:

I. N. Mihailescu, C. Ristoscu, F. Sima*“Soft pulsed laser technologies for transfer of organic materials”;* ; Invited lecture (I-08) at 13th International Conference on Laser Ablation (COLA 2015), August 31 – September 4, 2015, Cairns, Australia

Ion N. Mihailescu, C. Ristoscu; "*New results with pulsed laser technologies fir transfer of organic and biological substances : applications in biomedicine:'* Invited lecture (LM-I-20) at Conference on advanced Laser Technologies ALT 2015, September 7-11, 2015, Faro, Portugal

A.Visan, A. Janković, S. Eraković, C. Ristoscu, N. Mihailescu (Serban), L. Duta, G.E.Stan, A.C.Popa, M.A. Husanu, C.R. Luculescu, V.V. Srdić, Dj. Janaćkovic;*“Structural and biological characterization of lignin incorporation to simple and silver-doped hydroxyapatite coatings synthesized by matrix-assisted pulsed laser evaporation”;* Poster presentation (CC.PI 33) at E-MRS 2015, May 11-15, 2015, Lille, France

Date,

Project Director,

Prof. Dr. Ion N. Mihailescu

December 15, 2015